Ligand-centered hydrogen evolution with Ni(II) and Pd(II)DMTH

Christine A. Phipps,[a] Dillon T. Hofsommer,[a] Megan J. Toda,[a] Francois Nkurunziza,[b] Bhoomi Shah,[a] Joshua M. Spurgeon,[b] Pawel M. Kozlowski,[a] Robert M. Buchanan,[a] Craig A. Grapperhaus*[a]*

[a] Department of Chemistry, University of Louisville, Louisville, KY, 40292, United States

[b] Conn Center for Renewable Energy Research, University of Louisville, Louisville, KY, 40292, United States

Abstract

In this study we report a pair of electrocatalysts for the hydrogen evolution reaction (HER) based on the non-innocent ligand diacetyl-2-(4-methyl-3-thiosemicarbazone)-3-(2-pyridinehydrazone) (H_2DMTH, H_2L^1). The neutral complexes NiL^1 and PdL^1 were synthesized and characterized by spectroscopic and electrochemical methods. The complexes contain a non-coordinating, basic hydrazino nitrogen that is protonated during the HER. The pK_a of this nitrogen was determined by spectrophotometric titration in acetonitrile to be 12.71 for NiL^1 and 13.03 for PdL^1. Cyclic voltammograms of both NiL^1 and PdL^1 in acetonitrile exhibit diffusion-controlled, reversible ligand-centered events at -1.83 V and -1.79 V (vs. ferrocenium/ferrocene) for NiL^1 and PdL^1, respectively. A quasi-reversible, ligand-centered event is observed at -2.43 V and -2.34 V for NiL^1

and PdL^1, respectively. The HER activity in acetonitrile was evaluated using a series of neutral and cationic acids for each catalyst. Kinetic isotope effect (KIE) studies suggest the pre-catalytic event observed is associated with a proton coupled electron transfer step. The highest turnover frequency values observed were 6150 s^{-1} at an overpotential of 0.74 V for NiL^1 and 8280 s^{-1} at an overpotential of 0.44 V for PdL^1. Density functional theory (DFT) computations suggest both complexes follow a ligand-centered HER mechanism where the metals remain in the +2 oxidation state.

Introduction

The heavy use of fossil fuels has resulted in growing problems related to pollution and climate change.[1] This has stimulated greater use of alternative, renewable energy sources based on solar photovoltaics, wind, and water power.[2] Using these sources to generate hydrogen is an attractive and potentially sustainable approach as it offers an energy dense fuel with non-carbon emissions when combusted with O_2.[3] Platinum is the best catalysis for the electrochemical generation of H_2 via the hydrogen evolution reaction (HER), however its high cost and scarcity limit its practical use for large scale H_2 production.[4] As such, there has been considerable effort in the development of low cost electrocatalysts containing earth abundant metals as an alternative to Pt in electrolyzers.

Redox-active ligands are of special interest in HER because the ligand can act as an electron reservoir and facilitate two-electron activity with earth abundant, cost efficient first row transition metals in molecular catalysts.[5-7] For several years, we and others have evaluated Zn,[8-9] Cu,[10-12] Ni,[13-17] Pd,[18] and Co[19-20] complexes with redox active bis-thiosemicarbazones (BTSC) ligands (Figure 1) as electrocatalysts for the HER. The highly modular nature of BTSCs allows tuning of ligand electronics and basicity. Recently, we began exploring the electrocatalytic activity of the

related ligand diacetyl-2-(4-methyl-3-thiosemicarbazone)-3-(2-pyridinehydrazone) (H_2L^1) in which a thiosemicarbazone moiety is replaced with 2-pyridinehydrazone (Figure 1).[8]

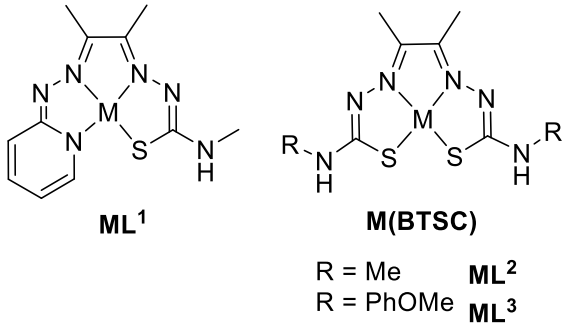

Figure 1. Structure of ML^1 and general M(BTSC) complexes.

The electrocatalytic HER activity of ZnL^1 includes transfer of both electrons and protons to the ligand. This cooperativity between the metal and non-innocent ligand can lead to different H_2 evolution pathways based on the specific metal-ligand combination. As shown for M(BSTC)s, pathways include: 1) metal-assisted ligand-centered, where the metal acts as an electron reservoir for bond making/breaking reactions at the ligand;[21-23] 2) ligand-assisted metal-centered, where the ligand is an electron reservoir supporting a metal hydride intermediate;[10, 24] and 3) ligand-centered, where the ligand alone is responsible for activity with the metal absent or in a structural role.[13, 16-18, 20] For ZnL^1, the reaction follows a ligand-centered pathway as the metal is redox inactive. Herein, we report the synthesis and characterization of the nickel(II) and palladium(II) derivatives, NiL^1 and PdL^1, and their respective HER activity in acetonitrile with three different acids. Acetonitrile was chosen as the solvent due to poor solubility of these rigidly planar species. The results show that a ligand-centered pathway is retained, despite the presence of redox-active metals.

Experimental

Materials and Methods

All solvents and materials were purchased from commercial sources as reagent grade and used as received. Solvents were dried using an MBraun solvent purification system. H_2L^1 was synthesized in high yield following a previously reported procedure.[11] Purity was confirmed by ^1H and ^{13}C NMR. Due to the slow relaxation of C=N bonds (1-40 seconds), some signals are absent in the ^{13}C NMR but are observed with the HMQC.[25] Pyridinium tetrafluoroborate, triethylammonium tetrafluoroborate, and $HDBU^+$ (1,8-diazabicyclo(5.4.0)undec-7-enium) tetrafluoroborate were prepared by a published procedure and stored in a desiccator.[26] Complexes in this study are air and water stable as solids and did not require protection from the atmosphere.

(diacetyl-2-(4-methyl-3-thiosemicarbazato)-3-(2-pyridinehydrazonato))nickel(II) NiL^1: H_2L^1 (438 mg, 1.66 mmol) and nickel (II) acetate (412 mg, 1.66 mmol) were suspended in 20 mL ethanol. The forest green slurry was heated to reflux for 1 hour, cooled to room temperature, and layered with ether. The resultant solid was filtered and washed with hexanes and dried on filter paper yielding 503 mg dark green solid (94% yield). Attempts to obtain single crystals for x-ray analysis through vapor diffusion, layering, and slow evaporation with a variety of organic solvents were unsuccessful. ^1H NMR (DMSO- *d_6*, 700 MHz, 343.15 K): 7.29 (H_7, s), 7.13 (H_3, td, 8 Hz), 6.36 (H_1, d, 6 Hz), 6.27 (H_4, d, 8 Hz), 5.99 (H_2, t, 6 Hz), 2.73 (H_8, d, 4 Hz), 1.79 (H_6, s), 1.75 (H_5, s) ppm. ^{13}C NMR (DMSO-*d_6*, 700 MHz, 343.15 K) δ: 171.8 (C_5), 171.1 (C_{10}), 159.8 (C_6), 148.8 (C_1), 144.3 (C_8), 139.5 (C_3), 110.8 (C_2), 110.4 (C_4), 31.1 (C_{11}), 12.5 (C_9), 11.1 (C_7) ppm. FT-IR (ATR): 3165 br, 2971 br, 1612 m, 1522 m, 1400 m, 1430 s, 1456m, 1272s, 1216 vs, 1148 w, 1115 w, 1080 m, 993 m, 842 w, 750 m, 726 w, 650 m cm^{-1}. Elemental analysis for $C_{11}H_{14}N_6SNi$ calc: C, 41.03; H, 4.70; N, 26.10. Found: C, 41.27; H, 4.59; N, 26.09. UV – visible spectrum (MeCN), λ_{max} (nm), (ε) ($M^{-1}cm^{-1}$): 369 (10600), 718 (2550).

(diacetyl-2-(4-methyl-3-thiosemicarbazato)-3-(2-pyridinehydrazonato))palladium(II)

PdL^1: Palladium (II) acetate (230 mg, 1.02 mmol) and H_2L^1 (275 mg, 1.04 mmol) were suspended in 20 mL methanol. The blue-green suspension was magnetically stirred for 30 minutes, heated to boil for 20 minutes, and cooled. The resultant solid was filtered, washed with 20 mL methanol and 40 mL ether and dried on the filter to obtain 191 mg dark blue-green solid (51% yield). Attempts to obtain single crystals for x-ray analysis through vapor diffusion, layering, and slow evaporation with a variety of organic solvents were unsuccessful. ^{1}H NMR (DMSO-*d*$_6$, 700 MHz, 343.15 K) δ: 7.32 (H_7, br s), 7.23 (H_3, t, 8 Hz), 7.04 (H_1, d, 6Hz), 6.48 (H_4, d, 9 Hz), 6.13 (H_2, t, 7 Hz), 2.78 (H_8, d, 3 Hz), 1.91 (H_6, s), 1.83 (H_5, s) ppm. ^{13}C NMR (DMSO-*d*$_6$, 700 MHz, 343.15 K) δ: 172.8 (C_5), 172.3 (C_{10}), 161.7 (C_8), 150.3 (C_1), 144.0 (C_6), 139.7 (C_3), 112.4 (C_4), 111.4 (C_2), 32.0 (C_{11}), 13.0 (C_9), 11.6 (C_7) ppm. FT-IR (ATR): 3157 br, 2950 br, 1608 w, 1508 m, 1452 m, 1425 s, 1396 s, 1348 w, 1296 vs, 1271 m, 1250 m, 1209 vs, 1147 m, 1124 m, 1072 s, 1034 w, 1011 s, 991 s, 903 w, 835 w, 746 s, 727 m, 646 s cm^{-1}. Elemental analysis for $C_{11}H_{14}N_6SPd$ calc: C, 35.83; H, 3.83; N, 22.79. Found: C, 35.91; H, 3.79; N, 22.82. UV – visible spectrum (MeCN), λ_{max} (nm), (ε) ($M^{-1}cm^{-1}$): 293 (4390), 696 (3880).

Physical Methods

Elemental analyses were performed by Midwest Microlab (Indianapolis, IN, USA) or Micro-Analysis Inc. (Wilmington, DE, USA) by combusting the sample on a calibrated microbalance based on the methodologies of Pregl (CH) and Dumas (N) (CHN: ASTM D5291). ^{1}H and NMR data were collected on a Varian Inova 500 MHz NMR spectrometer using deuterated solvents (Cambridge Isotopes). Infrared spectra were recorded on a Thermo Nicolet Avatar 360 spectrometer with an ATR attachment (4 cm^{-1} resolution).

pKa Determination

pK_a values were determined through spectrophotometric titration of the colored compound with a reference acid of known pK_a in MeCN to determine ΔpK_a values. Electronic adsorption spectra were recorded with an Agilent 8453 diode array spectrometer with a 1 cm path length quartz cell. The cuvette was filled with 2.0 mL of a stock solution of ML^1 and titrated with small quantities of a stock solution of pyridinium tetrafluoroborate (Figure 2 and S7), triethylammonium tetrafluoroborate, acetic acid, or $HDBU^+$ tetrafluoroborate. Pyridinium ($pK_{a,\ MeCN}$ = 12.53) was used for pK_a determinations as the titrant acid. See SI for example pK_a calculations.

Electrochemical Measurements

Cyclic voltammetry (CV) and controlled potential coulometry (CPC) data were collected using a Gamry 1040 E Interface potentiostat/galvanostat. Cyclic voltammograms were collected using a three-electrode cell with a glassy carbon working electrode, an Ag wire quasi-reference electrode, and a Pt wire counter electrode. The glassy carbon electrode (GCE) was polished prior to use with an aqueous alumina slurry. The electrodes were rinsed with water, acetone, acetonitrile, and air dried prior to use. The glassy carbon electrode was polished after each scan to remove any adhered substances. All CVs are referenced against ferrocenium/ferrocene (Fc^+/Fc^0) standard couple as an internal standard. In a typical electrochemical experiment, 0.15 mM of catalyst was dissolved in 25 mL of acetonitrile containing 0.1 M tetrabutylammonium hexafluorophosphate (Bu_4NPF_6) as the supporting electrolyte. The solution was sparged with argon for fifteen minutes to remove dissolved oxygen prior to data collection. After the addition of each aliquot of acid the solution was stirred for 15 seconds prior to data collection. CVs were recorded at a scan rate of 0.200 V/s. Scan rate independence was performed at 3, 3.5, and 4 V/s to calculate TOF following the method of Artero and coworkers (details in SI).[27] Overpotential was determined by the peak potential of the catalytic wave at acid saturation where the standard reduction potential was determined using

the methods of Artero et al. (details in SI).[27] The peak current was chosen to run the CPC at and determine overpotential because at that point the current is diffusion limited, rather than potential limited. The CPC measurements were conducted using an H-cell with the working and counter electrode compartments separated by a glass frit. The cell was cleaned with acetone and acetonitrile followed by an excessive rinse with deionized water and dried overnight in an oven (100°C). The working electrode compartment (cathode) contained a glassy carbon electrode, which was polished with an alumina slurry, and an Ag/AgCl reference electrode in a saturated KCl solution. The compartment was sealed with a Pine low volume cell cap, and the solution was sparged at a constant flow rate with Ar, which was vented to a gas chromatograph (GC) to detect and quantify hydrogen for faradaic efficiency (FE) determination. The counter electrode compartment contained a Pt mesh electrode. In a typical study, the working electrode compartment was loaded with 7 mL of 0.25 mM ML^1 solution containing 0.1 M Bu_4NPF_6 and acid at saturating conditions (Table S1) in acetonitrile and with a 0.1 M Bu_4NPF_6 solution in the counter electrode compartment. Both cell compartments were initially sparged with argon for 15 minutes and then kept under an argon atmosphere during data collection. The potential selected for CPC was determined from the $E_{cat/2}$ value. CPC measurements were background corrected using data collected with acid present but no catalyst.

Computational Studies

Density functional theory (DFT) was used to determine electronic and geometric properties of the Ni and Pd catalysts. The accuracy of DFT in comparing computational results with those obtained from experimental data is largely dependent on functional choice. To determine the proper functional for the present systems, a series of functionals were used to compare geometric parameters as well as redox potential and pK_a values. Functionals evaluated include: B3LYP,

B3P86, B3PW91, B97D, BP86, M06, M06-L, PBE0, TPSS, and ωB97XD. The 6-311g(d,p) basis set was used with each functional for the Ni species and the def2TZVP basis set was used for the Pd species. All calculations were performed using an acetonitrile solvation model. For the Ni species, a polarized continuum model (PCM) solvation model and solvation model based on density (SMD) were tested to determine if the redox potential was sensitive solvation. The SMD model produced redox potentials closer to experimental values. For the Pd catalyst, the PCM model was used as the redox potentials were closer to experimental values. Frequency calculations based on optimized geometries contained no imaginary frequencies. The DFT calculations were performed in Gaussian 16. Chemcraft and Gaussview were used for visualization and orbital rendering.

Results and Discussion

Synthesis and Characterization

The neutral complexes NiL^1 and PdL^1 were prepared by the reaction of H_2L^1 with the appropriate metal acetate salt in refluxing alcohol (Scheme 1). The protonated derivatives $[Ni(HL^1)]BF_4$ and $[Pd(HL^1)]BF_4$ were obtained upon addition of HBF_4 to methanol solutions of the metal complexes. All the complexes were characterized by FT-IR spectroscopy as solids (Figures S1 – S2). The spectrum of NiL^1 is consistent with the coordination of $(L^1)^{2-}$ to Ni(II) and displays a thioamide bending mode at 650 cm^{-1}, C=N thioamide stretching modes at 1522 and 1612 cm^{-1}, and an N-H stretch at 3165 cm^{-1}.[28] Upon protonation to $[Ni(HL^1)]BF_4$, a prominent B-F stretch is observed at 1060 cm^{-1} with a slight shift in the thioamide bend and the C=N and thioamide stretches shift to 1617, 1508 and 661 cm^{-1}. For $[Ni(HL^1)]BF_4$ *ν*NH stretches are observed at 3521 and 3301 cm^{-1}. The spectrum of PdL^1 and $[Pd(HL^1)]BF_4$ are similar to their nickel analogues and display bands at 646, 1508, 1608 and 3157 cm^{-1} and 648, 1580, 1677, 3392 and 3032 cm^{-1}, respectively.

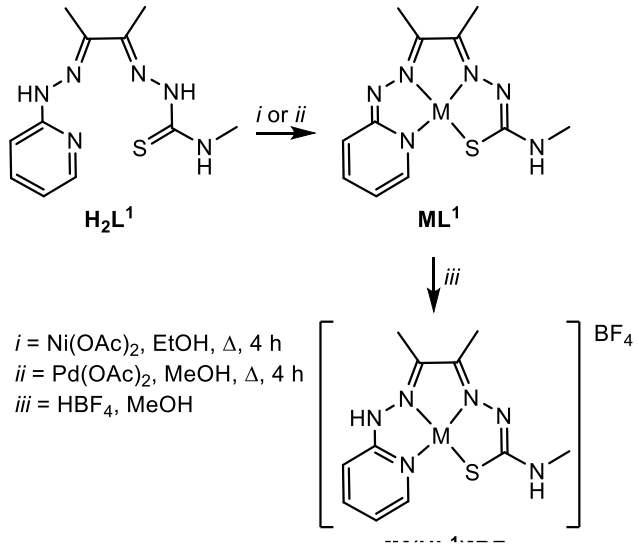

Scheme 1. Synthesis and protonation reaction scheme of NiL^1 and PdL^1.

The structures of the nickel and palladium complexes were further confirmed by ^1H NMR spectroscopy (Figures S3 – S4). All the complexes are diamagnetic as expected for square planar, d^8 metal ions. It should be noted that due to the rigid square planar geometry of these complexes they are poorly soluble in organic solvents so NMRs were recorded at 70° C. The ^1H NMR spectrum of NiL^1 in DMSO-d_6 shows a sharp, exchangeable singlet at 7.29 ppm assigned to the amino proton of N<u>H</u>CH_3. Four aromatic multiplets resonances appear between 5.99 and 7.13 ppm for the shielded pyridyl CH protons. A pair of singlets are observed at 1.77 and 1.79 ppm assigned to the protons of the α-diimine methyl groups. In addition, NHC<u>H</u>$_3$ methyl protons appear as a doublet at 2.73 ppm. Upon protonation all signals for $[Ni(HL^1)]^+$ shift downfield by an average of 0.4 ppm, closer to the resonances observed for H_2L^1.[29] The ^1H NMR spectrum of PdL^1 shows the same pattern as NiL^1, but the aromatic resonances are shifted further downfield by 0.1-0.2 ppm compared to NiL^1. The other proton signals for $[Pd(HL^1)]^+$ are shifted further downfield compared to $[Ni(HL^1)]^+$.

The electronic spectra of the nickel and palladium complexes were recorded in acetonitrile (Figures S5 – S6). The green solution of NiL^1 shows a low intensity d-d band at 718 nm and a more intense charge transfer band at 369 nm. Upon protonation with pyridinium, a color change to yellow is observed with an accompanying shift of the d-d band to 490 nm and a shift in the charge transfer band to 380 nm. The blue solution of PdL^1 exhibits similar characteristics with a low intensity d-d band at 696 nm and a charge transfer band at 293 nm. Protonation of PdL^1 yields a fuchsia-colored solution with a shifted d-d band at 559 nm and shifted a charge transfer band at 398 nm. The previously reported compound, ZnL^1, is similarly protonated by acetic acid on the non-coordinated hydrazine nitrogen with a concomitant color change from orange to yellow.[8]

To quantify the acid/base properties of the complexes, $pK_{a,MeCN}$ measurements were obtained through spectrophotometric titration of each compound in acetonitrile. Pyridinium tetrafluoroborate ($pK_{a,MeCN}$ = 12.53) was chosen because the poorly coordinating BF_4 counterions minimize ion pairing effects.[9] Titration of NiL^1 with pyridinium tetrafluoroborate produces a reversible color change from green to yellow with clean isosbestic points at 305 and 352 nm (Figure 2). A $pK_{a,MeCN}$ of 12.71 was determined for $[Ni(HL^1)]^+$. Similarly, a $pK_{a,MeCN}$ of 13.03 was determined for $[Pd(HL^1)]^+$ (Figure S7). Both complexes are more basic than the related BTSC complex, NiL^2, which was not protonated upon addition of acids such as trifluoroacetic acid.[21]

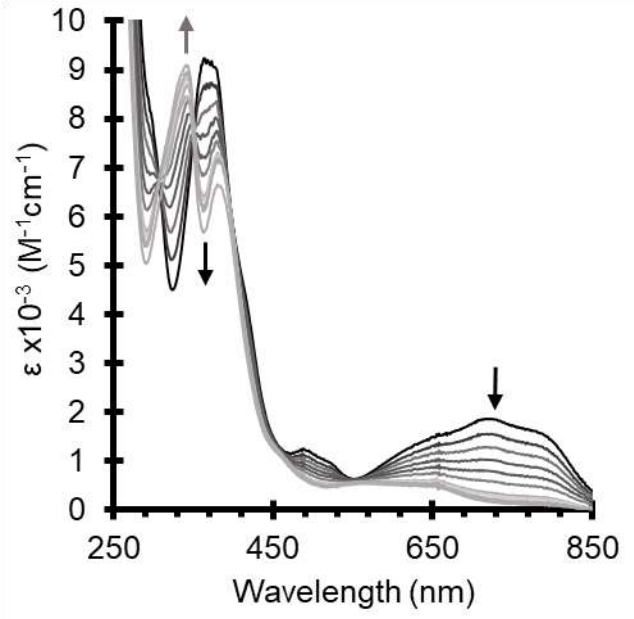

Figure 2. Spectrophotometric titration of NiL^1 with pyridinium tetrafluoroborate for the determination of ΔpK_a in acetonitrile from 0 eq. (black) to 5 eq. (gray)

NiL^1 and PdL^1 have remarkably similar cyclic voltammograms in MeCN (Figure 3). Both complexes display one reversible reduction event and a second, quasireversible reduction at -1.83 V and -2.43 V (versus ferrocenium/ferrocene, Fc^+/Fc) for NiL^1 and -1.79 V and -2.34 V for PdL^1. A daughter peak associated with the second reduction is observed at -1.12 V for NiL^1 and less prominently at -1.28 V for PdL^1. The potential vs. log(scan rate) (Cottrell) plots of the first reduction for each complex are linear at the scan rates employed (50 – 1000 mV/s) with diffusion coefficients of 7.37 x 10^{-5} cm^2 s^{-1} for NiL^1 and 9.44 x 10^{-5} cm^2 s^{-1} for PdL^1 (Figure S8 – S9). For both complexes, the reductions are assigned as ligand-centered based on computation studies (*vide infra*). The ligand in these Ni and Pd complexes therefore reduce at potentials ca. 600 mV more anodic compared to the related complex, ZnL^1, which displays a single, irreversible ligand-centered reduction at -2.47 V in MeCN.[8] Notably, the BTSC complex NiL^2 displays two quasi-reversible reductions at very similar potentials to NiL^1 (-1.73 V and -2.31 V in MeCN)[21], and NiL^3

has two similar events in DMF at -1.57 and -2.20 V vs. Fc^{+}/Fc.[17] For the BTSC complexes, the first redox event is attributed to a ligand-centered reduction and the second event is associated with a metal-centered reduction resulting in a triplet spin state. The Pd(BTSC) derivative PdL^3 also displays one ligand-centered and one metal-centered reduction similar to NiL^3.[18]

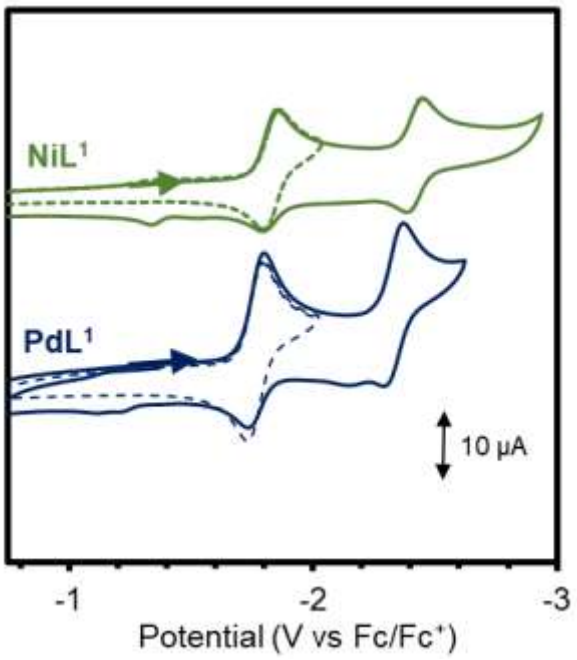

Figure 3. Cyclic voltammograms of 1 mM NiL^1 and PdL^1 in acetonitrile with 0.1 M tetrabutylammonium hexafluorophosphate at a scan rate of 200 mV/s. The dashed line is a sweep reversed prior to the second reduction, indicating the daughter peak is associated with the second reduction.

Electrocatalytic Hydrogen Evolution Reaction

The electrocatalytic HER activity of NiL^1 and PdL^1 was studied using three weak acids with a range of pK_a values: triethylammonium ($HNEt_3^+$, $pK_{a,MeCN} = 18.63$), acetic acid ($pK_{a,\,MeCN} = 23.51$), and 1,8-diazabicyclo[5.4.0]undec-7-ene ($HDBU^+$, $pK_{a,MeCN} = 24.34$)[26]. The selected acids have $pK_{a,MeCN}$ values greater than the metal catalysts which largely avoids protonation prior to reduction. This was confirmed by titration of NiL^1 and PdL^1 with a large excess with each of the

acids (Fig S10 - S15) to show no discernable change in the UV-visible spectra. Triethylammonium and $HDBU^+$ were especially chosen because they are bulky, cationic acids with low homoconjugation constants in acetonitrile. Use of these acids allows an evaluation of the effect of acid charge while avoiding the complication of homoconjugation, which affects the reactivity of acetic acid.[27]

The addition of $HDBU^+$ to NiL^1 in MeCN generates a catalytic wave near -2 V vs. Fc^+/Fc, and a precatalytic wave that is anodically shifted relative to the first reduction potential (Figure 4 and Figures S16 – S20). The catalytic to peak current ratio (i_{cat}/i_p) increased with increasing acid concentration until acid saturation conditions were reached at 21.4 mM. Under acid saturation conditions, the scan rate was increased until the scan rate independent region was observed at 3.0 V/s. Experiments with NiL^1 in the presence of $HNEt_3^+$ and acetic acid also displayed pre-catalytic waves at saturating conditions of 77.6 mM at 3.5 V/s and 1034 mM at 3.5 V/s, respectively (Figures S16 – S17, Table S1). The PdL^1 catalyst showed a pre-catalytic and catalytic HER event upon titration with each of the three acids with similar acid saturation conditions (Figure S18 – S20, Table S1).

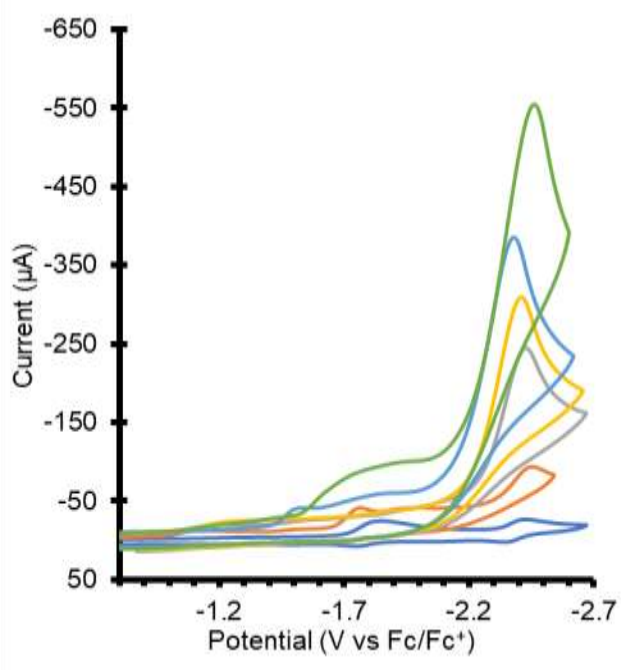

Figure 4. Cyclic voltammograms of 0.2 mM NiL^1 titrated with $HDBU^+$ in MeCN with 0.1 M tetrabutylammonium hexafluorophosphate) at a scan rate of 200 mV/s (dark blue = 0 eq.; red = 20 eq.; gray = 41 eq.; yellow = 48 eq.; light blue = 57 eq.; green = 107 eq.).

An overview of the TOF and overpotential for NiL^1 and PdL^1 with each of the three acids is provided in Figure 5. The presence of a pre-catalytic wave precluded quantification of TOF using foot-of-the-wave analysis.[30] Instead, the TOF was estimated from the i_{cat}/i_p ratio.[31] The overpotential (η) was calculated using the methods describe by Artero with inclusion of the effects of homoconjugation for acetic acid.[27] The data clearly shows that PdL^1 requires a lower overpotential than NiL^1 by 240 - 480 mV. The lowest overpotential, 260 mV, is observed for PdL^1 with acetic acid. The charged acids require an additional 200-240 mV of overpotential which may be due to ion pairing in solution or charge attraction following the first protonation.[26, 32] The same trend is observed with NiL^1 with the lowest overpotential, 640 mV, observed in MeCN with acetic acid. The TOF is highest for the strongest acid, $HNEt_3^+$, with values of 6200 s^{-1} and 2600 s^{-1} for

NiL^1 and PdL^1, respectively. The TOF follows a trend of decreasing with decreasing acid strength, regardless of charge. This is due to decreasing proton availability with increasing $pK_{a,MeCN}$. The turnover number (TON) was determined with $HNEt_3^+$ to be 8.05 and 3.18 for NiL^1 and PdL^1, respectively. In general, the TOF of NiL^1 is greater than PdL^1 with the important caveat that it requires a significantly higher overpotential. The activity of NiL^1 is similar to the BTSC complexes NiL^2 and NiL^3 which have reported TOFs of 4200 s^{-1} (η = 0.53 V)[21] and 3080 s^{-1} (η = 0.34 V),[17] respectively. The PdL^3 catalyst has a much lower TON of 2 s^{-1} with trifluoroacetic acid in DMF and a faradaic efficiency of 34%, where the low efficiencies are due to deposition of Pd nanoparticles.[18]

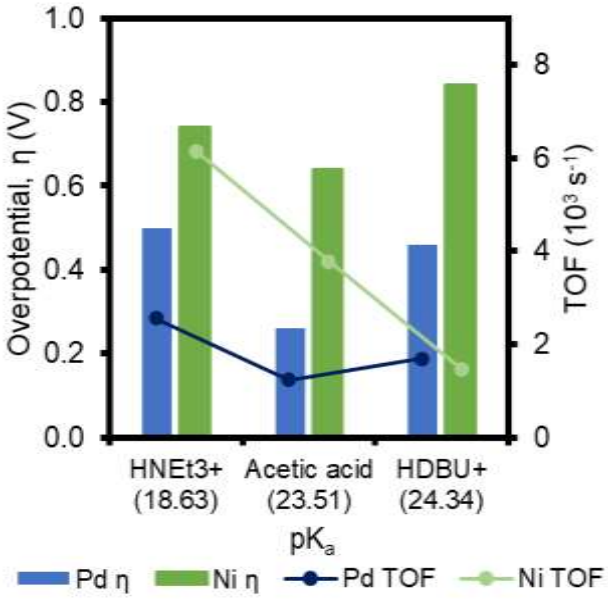

Figure 5. Comparison of overpotential and TOF to the acid pK_a.

Kinetic isotope effect (KIE) experiments were performed by electrocatalytic titration of the complexes in 0.2 M D_2O or H_2O solutions of acetonitrile with $HDBU^+$ and $HNEt_3^+$ following the method of Dempsey and coworkers.[33-34] The KIE values for the precatalytic and catalytic waves for NiL^1 with $HNEt_3^+$ are 3.7 and 2.6, respectively. The KIE value of the precatalytic wave is

consistent with a proton coupled mechanism and the value for the catalytic event indicates the proton is involved in the rate determining step.[33, 35] Similar KIE values were observed for NiL^1 with $HDBU^+$ and PdL^1 (Table S2). Interestingly, the BTSC complex NiL^2 displays an inverted KIE with a value of 0.75 attributed to a metal hydride and a ligand-assisted metal-centered mechanism. The KIE values for NiL^1 and PdL^1 are more like that of the BTSC complex ZnL^2, 1.2, which operates via a ligand-centered mechanism. Since NiL^3 is also reported to follow a ligand-centered mechanism, we synthesized NiL^3 according to literature methods[17] and measured a KIE for the catalytic wave of 2.1 with trifluoracetic acid (the acid NiL^3 was reported with).

Stability Studies

The CVs of NiL^1 and PdL^1 both exhibit curve crossing when the concentration of $HNEt_3^+$ exceeds 80 equivalents. Crossing behavior occurs when the kinetics in the forward sweep are slower than in the reverse sweep and may be indicative of film formation.[26, 33] Film formation has frequently been reported with M(BTSC) HER catalysts but there are no prior reports of curve crossing phenomenon.[8, 10, 14, 16-21] Sequential CV scans for both NiL^1 and PdL^1 under saturating conditions of $HNEt_3^+$ showed an anodic shift in the catalytic wave confirming film formation (Figure S21 – S25). The CVs of NiL^1 and PdL^1 with acetic acid and $HDBU^+$ also showed an anodic shift in the catalytic wave consistent with film formation after multiple scans, although curve crossing was not always observed.

To evaluate the activity of the films, two different rinse tests were performed. In the first test, a single CV of NiL^1 was scanned in the presence of $HNEt_3^+$. The electrode was then placed in a fresh solution of $HNEt_3^+$ without dissolved NiL^1. The current observed was 60% of the current observed in the first scan indicating the presence of an electroactive film. Similar experiments with acetic acid and $HDBU^+$ also showed film formation, although with 22% of the current of

homogeneous NiL^1. In the second rinse test, a solution containing NiL^1 and saturating $HNEt_3^+$ were scanned 10 times. The electrode was then placed in a fresh solution of $HNEt_3^+$ without dissolved NiL^1. The resulting current accounts for 98% of the previously observed current regardless of the acid. Similar results for both tests were obtained for PdL^1, concluding that these BTSC derivatives have non-negligible contribution from film formation on the observed faradaic efficiencies described below. Our mechanistic conclusions descried *vide infra* are of a single sweep to minimize film formation where most activity is attributed to the homogeneous ML^1. An electrocatalytically active film accounts for much of the activity in PdL^3, however most of the activity in NiL^3 is attributed to the homogeneous catalyst.[17, 36] NiL^2 can be deposited on a glassy carbon electrode following reductive cycling with comparable faradaic efficiency as the homogenous catalyst.[37]

To evaluate the catalytic performance over time, controlled potential coulometry (CPC) experiments were performed for 2 hours under a continuous stream of argon (Figures S26 – S29). The electrochemical cell was attached to a gas chromatograph for analysis of the headspace gas confirming H_2 as the reduction product. The electrocatalytic activities of both NiL^1 and PdL^1 were evaluated using $HNEt_3^+$ and $HDBU^+$ as acid sources. NiL^1 displayed faradaic efficiencies of 91% and 93%, respectively. PdL^1 had faradaic efficiencies of 96% and 98%, respectively (Figures S26-S29). The faradaic efficiencies are similar to NiL^2 (87%) and NiL^3 (80%) and higher than PdL^3 (34%) in non-aqueous solution.[17-18, 21] For intact NiL^2 deposited on glassy carbon electrodes as a heterogeneous catalyst, a faradaic efficiency of nearly 100% was observed in 0.5 M H_2SO_4.[37]

As film formation was observed in the cyclic voltammograms, we wanted to investigate the film deposited over the two-hour bulk electrolysis. Following the bulk electrolysis with the homogeneous catalyst the electrode was the then placed in a fresh H-cell with the same

concentration of acid and analyzed for H_2 faradaic efficiency. The film operates at 100% faradic efficiency for both NiL^1 and PdL^1, the efficiencies of the film is larger than the homogeneous catalyst because all electrons passed go to evolve hydrogen rather than depositing a film (Figures S26-S29). Comparing the moles of H_2 produced in the two experiments indicates that the film accounts for 49% and 100% of the hydrogen produced in the homogeneous experiments with NiL^1 and PdL^1, respectively. Interestingly, this is similar to the findings of Straistari et al. where NiL^3 had some activity from the film while the film in PdL^3 was responsible for almost all the activity.[17-18] From this, all following mechanistic discussion is looking at the activity under a single sweep where we can assume the homogeneous catalyst is responsible for catalysis.

Computational Investigation

To further understand the reactivity of the homogeneous NiL^1 and PdL^1 and the HER mechanism, a series of geometry optimization studies on key intermediates in various protonation and charge states were conducted with DFT. The B3P86 functional and TZVP basis set gave the best match with experimental data (Table S3). This level of theory has been shown to be reliable in similar complexes.[38-39] The calculations were carried out in an acetonitrile solvent model employing SMD for NiL^1 and PCM for PdL^1. The thermodynamic feasibility of protonation and reduction events was evaluated by the calculation of equilibrium constants (K_{eq}) and reduction potential ($E_{1/2}$), respectively. The thermodynamic parameter K_{eq} was calculated by optimizing products and reactants and utilizing both $HNEt_3^+$ and $HNEt_3$ as independent calculations (results were similar across all 3 acids). The thermodynamic parameter $E_{1/2}$ was calculated using a direct reference to ferrocene and a Born−Haber cycle.[40-41] A summary of the calculations and a comparison of calculated versus experimental reduction potentials can be found in the sample calculations and Table S1.

The catalyst NiL^1 was optimized in three different charge states: NiL^1 ($S = 0$ or 1, $q = 0$), $[NiL^1]^-$ ($S = 1/2$, $q = -1$), and $[NiL^1]^{2-}$ ($S = 0$ or 1 $q = -2$), where S refers to overall spin. For NiL^1 and $[NiL^1]^{2-}$ the singlet spin states were lower than the triplet spin states by 19 and 28 kcal/mol, respectively. Based on the energy optimizations, the calculated reduction potentials for the $[NiL^1]^{0/-}$ and $[NiL^1]^{-/2-}$ couples are -1.61 and -2.47 V, which are consistent with the experimental values of -1.83 and -2.43 V (Figure 2). Both reductions are best described as ligand-centered based on the optimized structures and spin density plots showing the Ni and Pd have 2.1% and 6.2% spin density, respectively (Figures S39 and S40, Tables S5 and S6). The neutral complex NiL^1 is planar consistent with Ni(II) and a dianionic ligand. Bond distances and angles (Table S4) are similar to NiL^2 and ZnL^1.[8, 21] The one-electron reduced species, $[NiL^1]^-$, is a doublet with a majority (90%) of the spin density on the ligand. As expected for a formally Ni(II) complex, the d_{z2} orbital (LUMO +1) is vacant. The two-electron reduced species $[NiL^1]^{2-}$ could be described as Ni(II) with a fully reduced $(L^1)^{4-}$ ligand or Ni(0) with $(L^1)^{2-}$. The former assignment is preferred as d_{z2} orbital (LUMO +1) remains vacant and the inter-ligand bond distances are consistent with reduction of the ligand to a tetra-anion (Table S4). Calculations on PdL^1 yielded similar results consistent with the assignment of the $[PdL^1]^{0/-}$ and $[PdL^1]^{-/2-}$ couples as ligand-centered reductions (*Supporting Information*). The results contrast with NiL^2, NiL^3, and PdL^3 for which the first reduction was ligand-centered but the second reduction was metal-centered associated with a triplet ground state.[17-18, 21]

Next, the protonation of NiL^1 was explored at multiple sites including N^1, N^2, N^3, and N^4 (Figure 6). The lowest energy site of protonation for the neutral complex NiL^1 is at the non-coordinating pyridinylhydrazone nitrogen N^2, which is 5.24 kcal/mol more favorable than protonation of the uncoordinated hydrazino nitrogen of the thiosemicarbazone, N^4. Calculations with protonation of

the sulfur or nickel were difficult to optimize regardless of the restrictions placed on the calculation and the energies were 40-50 kcal higher than the lowest energy states when optimization was realized. The calculated pK_a associated with the N^2 site is 13.18, which is close to the experimental value of 12.73. Protonation shifts the first reduction by +550 mV relative to the $[NiL]^{0/-}$ with a calculated potential for the $[Ni(HL)]^{+/0}$ couple of -1.06 V.

Protonation of the reduced species $[NiL^1]^-$ and $[NiL^1]^{2-}$ was also explored at various sites. For $[NiL^1]^-$, N^2 remains the most basic site with an associated pK_a of 22.47. The potential for the $[Ni(HL)]^{0/-}$ couple, -1.88 V, is shifted by +590 mV relative to $[NiL]^{-/2-}$. Addition of a second proton to Ni(HL) prior to reduction is most favorable at N^4 than protonation at N^1 by 4.79 kcal/mol. The associated pK_a values are 14.78 and 11.27 for protonation at N^4 and N^1, respectively. Notably, for the two-electron reduced species $[Ni(HL^1)]^-$, the N^1 site is the most basic with associated pKa of 29.22. The N^3 site has similar basicity, pKa = 28.66, but the N^1 site is significantly less basic, pKa = 24.16. Overall, $Ni(H_2L_1)$ is best described as Ni(II) with a reduced ligand protonated at the adjacent N^1 and N^2 sites associated with the hydrazinopyridine functional group (Figure 6).

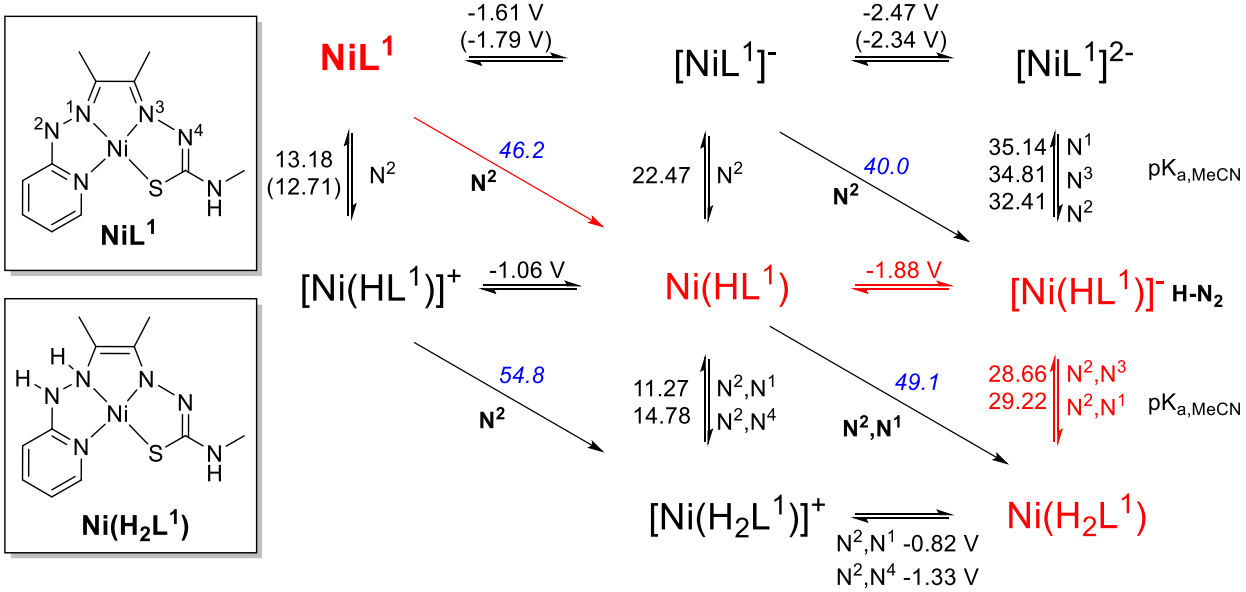

Figure 6. Representative square scheme of NiL^1 with [$HNEt_3^+$]. Experimental values are listed in parenthesis where applicable, all other values are calculated from DFT. Values over horizontal arrows represent reduction potentials (versus Fc^+/Fc). Values to the left of vertical arrows represent pK_a values for the associated position indicated on the right. Diagonal values are bond dissociation free energies (BDFE) values calculated as BDFE (kcal mol^{-1}) = 1.37 pK_a + 23.06 $E_{1/2}$ +52.6.[42]

Proposed HER Pathway

The red trace in Figure 6 highlights the preferred [EC]EC pathway from NiL^1 to the presumed homogeneous hydrogen evolving complex $Ni(H_2L_1)$ under our single sweep experimental conditions using weak acids with pKa values of 18.63 to 24.34. The pathway is thermodynamically consistent with the experimental and computed reduction potentials and pKa values. The first step is proton-coupled electron transfer (PCET) yielding $Ni(HL^1)$. The acids employed are not strong enough for a protonation of NiL^1 and the precatalytic wave occurs prior to the $[NiL^1]^{0/-}$ reduction potential. The PCET assignment is supported by the KIE values of the precatalytic wave. The next step is reduction of $Ni(HL^1)$ to $[Ni(HL^1)]^-$, which has a calculated reduction potential of $Ni(HL^1)$ is -1.88 V near the observed $E_{cat/2}$ for NiL^1 (Table S1). Reduction to $[Ni(HL^1)]^-$ facilitates the addition of a second proton at N^1 yielding the hydrogen evolving complex $Ni(H_2L^1)$.

The structure of $Ni(H_2L^1)$ is similar to that of the proposed hydrogen evolving complex for the BTSC catalyst CuL^2.[24] That complex follows a metal-assisted ligand-centered mechanism in which the hydrogen evolving complex $Cu(H_2L^2)$ is protonated at adjacent N sites on a thiosemicarbazone. Having both N^1 and N^2 protonated proved to be the lowest energy state, as seen in PdL^3.[18] While N^4 is close in pK_a and energy, the modest overpotential makes it unlikely there is intramolecular proton rearrangement as was seen in ZnL^1 with an overpotential of 1.2V.

Conclusions

Small changes to the ligand framework can alter both the electronic properties of the metal complex and which mechanism is active during electrocatalytic conditions. Notably, when the HER activity of a related BTSC complex, NiL^2, was characterized by Jain et. al., the key intermediate is a metal hydride.[21] The related complexes, NiL^3 and PdL^3, were shown by Orio and co-workers to undergo a metal assisted ligand-centered, and ligand-centered, respectively, mechanisms for HER.[36] Interestingly, PdL^3 showed not only a low TON (2 s^{-1}) and a low faradaic efficiency (FE) (34%); whereas NiL^3 is a better homogeneous catalyst with a TOF of 3080 s^{-1} and an 80% FE. Whereas the mechanism for M(BSTC)s has been shown to vary from metal-assisted ligand-centered, to ligand-assisted metal-centered, or ligand-centered depending on the identity of the metal and ligand substituents, to date the ML^1 complexes only show a ligand-only mechanism. Whether this holds true for metals beyond Ni, Pd, and Zn or with modification of the substituents on L^1 remains to be determined.

This study demonstrates how slightly modifying the electronic structure of a catalyst changes the mechanism. BTSCs are highly modular ligand structures and replacing a thiosemicarbazide moiety with a better sigma donor, hydrazinopyridine, results in a contraction of the xy plane. This contraction increases the energy of the d_{x2-y2} orbital enough to favor reducing the ligand twice rather than reducing the metal and the ligand, as seen in BTSCs (Figure 7). ML^1 in this study corresponds to a singlet when doubly reduced whereas NiL^2, NiL^3, and PdL^3 are all triplets due to the smaller energy gap between the ligand orbital and the d_{x2-y2} orbitals. All HER activity occurs on the hydrazinopyridine side of the ligand in NiL^1, PdL^1, and ZnL^1 and tuning the thiosemicarbazide side could make the reduction potentials more accessible potentially decreasing the overpotential of HER.

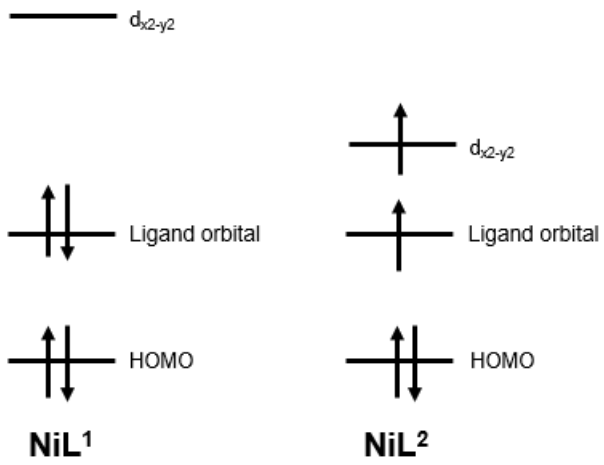

Figure 7. Orbital diagram showing the difference between NiL^1 and NiL^2.

References

1. Abe, J. O.; Popoola, A. P. I.; Ajenifuja, E.; Popoola, O. M., Hydrogen energy, economy and storage: Review and recommendation. *Int. J. Hydrogen Energy* **2019,** *44*, 15072-15086.
2. Midilli, A.; Ay, M.; Dincer, I.; Rosen, M. A., On hydrogen and hydrogen energy strategies: I: current status and needs. *Renew. Sust. Energ. Rev.* **2005,** *9*, 255-271.
3. Hwang, H. T.; Varma, A., Hydrogen storage for fuel cell vehicles. *Curr. Opin. Chem. Eng.* **2014,** *5*, 42-48.
4. Demirdöven, N.; Deutch, J., Hybrid Cars Now, Fuel Cell Cars Later. *Science* **2004,** *305*, 974-976.
5. Chirik, P. J.; Wieghardt, K., Radical ligands confer nobility on base-metal catalysts. *Science* **2010,** *327*, 794-795.
6. Upadhyay, A.; Meena, H.; Jha, R. K.; Kanika; Kumar, S., Isolation of monomeric copper(ii) phenolate selenoether complexes using chelating ortho-bisphenylselenide-phenolate ligands and their electrocatalytic hydrogen gas evolution activity. *Dalton Trans.* **2022,** *51*, 7284-7293.
7. Upadhyay, A.; Saurav, K. V.; Varghese, E. L.; Hodage, A. S.; Paul, A.; Awasthi, M. K.; Singh, S. K.; Kumar, S., Proton reduction by a bimetallic zinc selenolate electrocatalyst. *RSC Adv.* **2022,** *12*, 3801-3808.
8. Cronin, S. P.; Mamun, A. A.; Toda, M. J.; Mashuta, M. S.; Losovyj, Y.; Kozlowski, P. M.; Buchanan, R. M.; Grapperhaus, C. A., Utilizing Charge Effects and Minimizing Intramolecular Proton Rearrangement to Improve the Overpotential of a Thiosemicarbazonato Zinc HER Catalyst. *Inorg. Chem.* **2019,** *58*, 12986-12997.
9. Du, J.; Yang, H.; Wang, C.-L.; Zhan, S.-Z., A bis(thiosemicarbazonato)-zinc complex, an electrocatalyst for hydrogen evolution and oxidation via ligand-assisted metal-centered reactivity. *Appl. Organomet. Chem. n/a*, e6572.
10. Calvary, C.; Hietsoi, O.; Hofsommer, D.; Brun, H.; Costello, A.; Mashuta, M.; Spurgeon, J.; Buchanan, R.; Grapperhaus, C., Copper bis(thiosemicarbazone) Complexes with

Pendent Polyamines: Effects of Proton Relays and Charged Moieties on Electrocatalytic HER. *Eur. J. Inorg. Chem.* **2020,** *2021*.
11. Cowley, A. R.; Dilworth, J. R.; Donnelly, P. S.; White, J. M., Copper Complexes of Thiosemicarbazone−Pyridylhydrazine (THYNIC) Hybrid Ligands: A New Versatile Potential Bifunctional Chelator for Copper Radiopharmaceuticals. *Inorg. Chem.* **2006,** *45*, 496-498.
12. Calvary, C. A.; Hietsoi, O.; Hofsommer, D. T.; Brun, H. C.; Costello, A. M.; Mashuta, M. S.; Spurgeon, J. M.; Buchanan, R. M.; Grapperhaus, C. A., Copper bis(thiosemicarbazone) Complexes with Pendent Polyamines: Effects of Proton Relays and Charged Moieties on Electrocatalytic HER. *Eur. J. Inorg. Chem.* **2021,** *2021*, 267-275.
13. Barrozo, A.; Orio, M., Unraveling the catalytic mechanisms of H2 production with thiosemicarbazone nickel complexes. *RSC Adv.* **2021,** *11*, 5232-5238.
14. Calvary, C. A.; Hietsoi, O.; Strain, J. M.; Mashuta, M. S.; Spurgeon, J. M.; Buchanan, R. M.; Grapperhaus, C. A., Synthesis, Characterization, and HER Activity of Pendant Diamine Derivatives of NiATSM. *Eur. J. Inorg. Chem.* **2019,** *2019*, 3782-3790.
15. Panagiotakis, S.; Landrou, G.; Nikolaou, V.; Putri, A.; Hardré, R.; Massin, J.; Charalambidis, G.; Coutsolelos, A. G.; Orio, M., Efficient Light-Driven Hydrogen Evolution Using a Thiosemicarbazone-Nickel (II) Complex. *Front. Chem.* **2019,** *7*.
16. Papadakis, M.; Barrozo, A.; Straistari, T.; Queyriaux, N.; Putri, A.; Fize, J.; Giorgi, M.; Réglier, M.; Massin, J.; Hardré, R.; Orio, M., Ligand-based electronic effects on the electrocatalytic hydrogen production by thiosemicarbazone nickel complexes. *Dalton Trans.* **2020,** *49*, 5064-5073.
17. Straistari, T.; Fize, J.; Shova, S.; Réglier, M.; Artero, V.; Orio, M., A Thiosemicarbazone–Nickel(II) Complex as Efficient Electrocatalyst for Hydrogen Evolution. *ChemCatChem* **2017,** *9*, 2262-2268.
18. Straistari, T.; Hardré, R.; Massin, J.; Attolini, M.; Faure, B.; Giorgi, M.; Réglier, M.; Orio, M., Influence of the Metal Ion on the Electrocatalytic Hydrogen Production by a Thiosemicarbazone Palladium Complex. *Eur. J. Inorg. Chem.* **2018,** *2018*, 2259-2266.
19. Kaeffer, N.; Morozan, A.; Fize, J.; Martinez, E.; Guetaz, L.; Artero, V., The Dark Side of Molecular Catalysis: Diimine–Dioxime Cobalt Complexes Are Not the Actual Hydrogen Evolution Electrocatalyst in Acidic Aqueous Solutions. *ACS Catal.* **2016,** *6*, 3727-3737.
20. Straistari, T.; Hardré, R.; Fize, J.; Shova, S.; Giorgi, M.; Réglier, M.; Artero, V.; Orio, M., Hydrogen Evolution Reactions Catalyzed by a Bis(thiosemicarbazone) Cobalt Complex: An Experimental and Theoretical Study. *Chem. Eur. J.* **2018,** *24*, 8779-8786.
21. Jain, R.; Mamun, A. A.; Buchanan, R. M.; Kozlowski, P. M.; Grapperhaus, C. A., Ligand-Assisted Metal-Centered Electrocatalytic Hydrogen Evolution upon Reduction of a Bis(thiosemicarbazonato)Ni(II) Complex. *Inorg. Chem.* **2018,** *57*, 13486-13493.
22. Calvary, C.; Hietsoi, O.; Strain, J.; Mashuta, M.; Spurgeon, J.; Buchanan, R.; Grapperhaus, C., Synthesis, Characterization, and HER Activity of Pendant Diamine Derivatives of NiATSM. *Eur. J. Inorg. Chem.* **2019,** *2019*.
23. Aimoto, Y.; Koshiba, K.; Yamauchi, K.; Sakai, K., A family of molecular nickel hydrogen evolution catalysts providing tunable overpotentials using ligand-centered proton-coupled electron transfer paths. *Chem. Commun.* **2018,** *54*, 12820-12823.

24. Haddad, A. Z.; Cronin, S. P.; Mashuta, M. S.; Buchanan, R. M.; Grapperhaus, C. A., Metal-Assisted Ligand-Centered Electrocatalytic Hydrogen Evolution upon Reduction of a Bis(thiosemicarbazonato)Cu(II) Complex. *Inorg. Chem.* **2017,** *56*, 11254-11265.
25. Becker, E. D.; Shoup, R., 13C NMR spectroscopy: relaxation times of 13C and methods for sensitivity enhancement. *Pure Appl. Chem.* **1972,** *32*, 51-66.
26. McCarthy, B. D.; Martin, D. J.; Rountree, E. S.; Ullman, A. C.; Dempsey, J. L., Electrochemical Reduction of Brønsted Acids by Glassy Carbon in Acetonitrile—Implications for Electrocatalytic Hydrogen Evolution. *Inorg. Chem.* **2014,** *53*, 8350-8361.
27. Fourmond, V.; Jacques, P.-A.; Fontecave, M.; Artero, V., H2 Evolution and Molecular Electrocatalysts: Determination of Overpotentials and Effect of Homoconjugation. *Inorg. Chem.* **2010,** *49*, 10338-10347.
28. Desseyn, H. O.; Van Der Veken, B. J.; Herman, M. A., The Characteristic Pattern of Thioamides in Infrared and Raman Spectra. *Appl. Spectrosc.* **1978,** *32*, 101-105.
29. Calatayud, D. G.; Lopez-Torres, E.; Dilworth, J. R.; Antonia Mendiola, M., Complexes of group 12 metals containing a hybrid thiosemicarbazone-pyridylhydrazone ligand. *Inorg. Chim. Acta* **2012,** *381*, 150-161.
30. Costentin, C.; Drouet, S.; Robert, M.; Savéant, J. M., Turnover numbers, turnover frequencies, and overpotential in molecular catalysis of electrochemical reactions. Cyclic voltammetry and preparative-scale electrolysis. *J. Am. Chem. Soc.* **2012,** *134*, 11235-42.
31. Li, X.; Lei, H.; Liu, J.; Zhao, X.; Ding, S.; Zhang, Z.; Tao, X.; Zhang, W.; Wang, W.; Zheng, X.; Cao, R., Carbon Nanotubes with Cobalt Corroles for Hydrogen and Oxygen Evolution in pH 0–14 Solutions. *Angew. Chem. Int. Ed.* **2018,** *57*, 15070-15075.
32. Rountree, E. S.; Dempsey, J. L., Potential-Dependent Electrocatalytic Pathways: Controlling Reactivity with pKa for Mechanistic Investigation of a Nickel-Based Hydrogen Evolution Catalyst. *J. Am. Chem. Soc.* **2015,** *137*, 13371-13380.
33. McCarthy, B. D.; Donley, C. L.; Dempsey, J. L., Electrode initiated proton-coupled electron transfer to promote degradation of a nickel(II) coordination complex. *Chem Sci* **2015,** *6*, 2827-2834.
34. Costentin, C.; Robert, M.; Savéant, J.-M., Concerted proton–electron transfers in the oxidation of phenols. *Phys. Chem. Chem. Phys.* **2010,** *12*, 11179-11190.
35. Edwards, S. J.; Soudackov, A. V.; Hammes-Schiffer, S., Analysis of Kinetic Isotope Effects for Proton-Coupled Electron Transfer Reactions. *J. Phys. Chem. A* **2009,** *113*, 2117-2126.
36. Straistari, T.; Hardré, R.; Massin, J.; Attolini, M.; Faure, B.; Giorgi, M.; Réglier, M.; Orio, M., Influence of the Metal Ion on the Electrocatalytic Hydrogen Production by a Thiosemicarbazone Palladium Complex *Eur. J. Inorg. Chem.* **2018,** *2018*, 2061-2061.
37. Gupta, A. J.; Vishnosky, N. S.; Hietsoi, O.; Losovyj, Y.; Strain, J.; Spurgeon, J.; Mashuta, M. S.; Jain, R.; Buchanan, R. M.; Gupta, G.; Grapperhaus, C. A., Effect of Stacking Interactions on the Translation of Structurally Related Bis(thiosemicarbazonato)nickel(II) HER Catalysts to Modified Electrode Surfaces. *Inorg. Chem.* **2019,** *58*, 12025-12039.
38. Anjali, B. A.; Sayyed, F. B.; Suresh, C. H., Correlation and Prediction of Redox Potentials of Hydrogen Evolution Mononuclear Cobalt Catalysts via Molecular Electrostatic Potential: A DFT Study. *J. Phys. Chem. A* **2016,** *120*, 1112-1119.

39. Sciortino, G.; Lihi, N.; Czine, T.; Maréchal, J.-D.; Lledós, A.; Garribba, E., Accurate prediction of vertical electronic transitions of Ni(II) coordination compounds via time dependent density functional theory. *Int. J. Quantum Chem* **2018,** *118*, e25655.
40. Marenich, A. V.; Ho, J.; Coote, M. L.; Cramer, C. J.; Truhlar, D. G., Computational electrochemistry: prediction of liquid-phase reduction potentials. *Phys. Chem. Chem. Phys.* **2014,** *16*, 15068-15106.
41. Ding, S.; Ghosh, P.; Darensbourg, M. Y.; Hall, M. B., Interplay of hemilability and redox activity in models of hydrogenase active sites. *Proc. Natl. Acad. Sci. U. S. A.* **2017,** *114*, E9775-E9782.
42. Warren, J. J.; Tronic, T. A.; Mayer, J. M., Thermochemistry of Proton-Coupled Electron Transfer Reagents and its Implications. *Chem. Rev.* **2010,** *110*, 6961-7001.

ASSOCIATED CONTENT

Supporting Information.

The following files are available free of charge.

Sample calculations, IR, 1H NMR, UV-vis, Cottrell plots, cyclic voltammograms, bulk electrolysis, proton trees, and data summary are included (PDF).

AUTHOR INFORMATION

Corresponding Author

Craig Grapperhaus email: craig.grapperhaus@louisville.edu

Robert Buchanan email: robert.buchanan@louisville.edu

Author Contributions

F.N. performed bulk electrolysis experiments for Faradaic efficiencies. B.S. synthesized starting materials. M.J.T. and P.M.K. performed DFT calculations and delivered energies to C.A.P. C.A.P. performed all other experiments, interpreted DFT, and wrote the bulk of the manuscript. D.T.H., R.M.B., J.M.S., and C.A.G. conceived the project, supervised experimental studies, and

contributed to writing the manuscript. All authors have approved the final version of the manuscript.

Funding Sources

This research was supported by the National Science Foundation (CHE-1955268).

Notes

The authors declare no competing financial interests.

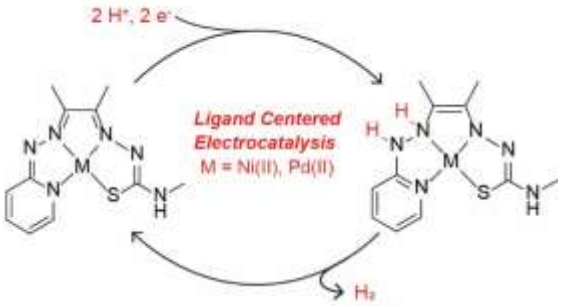

The neutral complexes NiL^1 and PdL^1 catalyze the electrochemical reduction of protons to hydrogen via a ligand centered pathway involving a redox activity of the ligand and protonation of a non-coordinating nitrogen basic site that is proximal to the ligand. The activity and mechanism is compared with related bis(thiosemicarbazone) complexes showing how the modular ligand structure can be used to tune reactivity and alter the reaction mechanism.